UKAEA-CCFE-PR(19)29

A.C. Field, L.N. Carter, N.J.E. Adkins, M.M. Attallah,
M.J. Gorley, M. Strangwood

The effect of powder characteristics on build quality of high purity tungsten produced via Laser Powder Bed Fusion (LPBF)

The effect of powder characteristics on build quality of high purity tungsten produced via Laser Powder Bed Fusion (LPBF)

A.C. Field, L.N. Carter, N.J.E. Adkins, M.M. Attallah, M.J. Gorley,
M. Strangwood

The effect of powder characteristics on build quality of high purity tungsten produced via Laser Powder Bed Fusion (LPBF)

A.C. Field[1,2], L.N. Carter[1], N.J.E. Adkins[1], M.M. Attallah[1], M.J. Gorley[2], M. Strangwood[1]
[1]School of Metallurgy & Materials, University of Birmingham, Edgbaston, B15 2TT, U.K.
[2]UK Atomic Energy Authority, Culham Science Centre, Abingdon, Oxfordshire, OX14 3DB, U.K.

Two high purity tungsten powders, produced via different manufacturing techniques, were characterized to determine size distribution, morphology, thermal properties and flow characteristics and thus, the likely suitability for Laser Powder Bed Fusion (LPBF) production. Specimens from duplicate builds were produced with the two powders and characterized for density, defect mechanisms and thermal penetration into the substrate plate to compare apparent power densities.

The first powder was a chemically reduced powder with irregular morphology and the second, a plasma spheroidized powder with highly spherical morphology. The latter was found to have tighter morphological control and size distribution, having a third of particles at the modal particle size in comparison to a fifth of the reduced powder. This led to better flow characteristics, and an increase of 1.5 gcm^{-3} (1500 kg m^{-3}) in the packing densities seen in the powder bed which corresponds to 57 % theoretical density versus 50 % theoretical density in the chemically reduced powder.

As a result, the specimens produced from the plasma spheroidized powder had higher densities (97.3 % vs. 88.5 %) and the dominant defect mechanism moved from lack of fusion dominated in the chemically reduced powder to cracking dominated in the plasma spheroidized. The plasma spheroidized powder also showed higher apparent power densities as evidenced by an 80 % deeper penetration of the laser into the substrate plate.

I. Introduction:

Tungsten is a candidate material for the plasma facing components (PFCs) within a nuclear fusion reactor as a result of its high melting point (3422 °C, 3695 K), high thermal conductivity (164 Wm^{-1}K^{-1}) and high density (19300 kg m^{-3})[1]. These allow the components to survive the operating temperatures as well as providing effective radiation shielding and conduction of heat through the components. The comparatively low activation of tungsten means that long term waste storage does not need to be considered and recycling methods are possible after 75 years [2].

There are difficulties associated with the processing of tungsten however, as a result of its high melting point and intrinsic brittleness (Ductile-Brittle Transition Temperature (DBTT) ~400 °C, 673 K) [3]. Conventionally, powder metallurgy methods including sintering have been used, but as final machining is challenging, the complexity of component geometries has been limited [4]. The current divertor monoblock design can be seen in Figure 1; its simple shape is largely dictated by manufacturing issues.
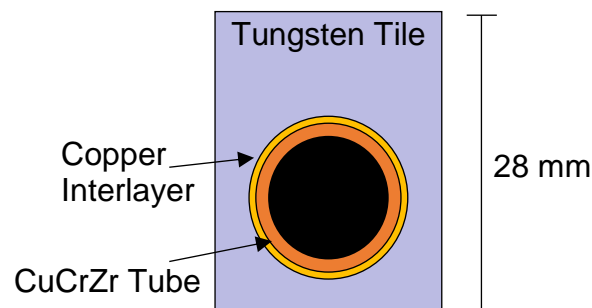

Figure 1 - Schematic representation of a divertor monoblock

Additive manufacturing techniques including Laser Powderbed Fusion (LPBF) offer the potential to produce components with greater complexity, such as small internal cooling channels, and without the need for low melting point binders or sintering aids (e.g. Cu, Ni) [5]. Early attempts at LPBF of tungsten-based materials investigated additions of these sintering aids which acted as a binder

phase, lowering the melting point and increasing processability so that densities of around 80 % with little cracking were achieved processing at 100 W [6, 7]. The high activation of Cu and Ni makes this strategy unsuitable for fusion applications. Attempts at processing both pure tungsten and molybdenum yielded low densities (<85 %) due to the low laser powers (<200 W) used [8, 9] resulting in incomplete consolidation. More recent work, conducted with 300 - 500 W systems have shown improved results with densification up to 96 % of theoretical density (TD), but suggested that cracking may be present [10, 11]. Densities of 96 % are significantly higher than previous attempts, but are still lower than those achievable in LPBF of conventional materials such as 316L where densities in excess of 99.5 % are possible [12].

Within radiation shielding applications, it is generally known that increasing the density of a material improves its shielding effect [13], as a result, improved densities are of importance to the successful implementation of LPBF technologies for the production of refractory metals. However, the presence of cracking as a result of fabrication would be detrimental in terms of stress concentrators and crack propagation and therefore an optimum may exist where a small amount of residual porosity exists.

Figure 2 summarizes the main input parameters affecting final build quality; these can be nominally divided into laser parameters, environment and powder characteristics. Of interest in this study is the effect of powder characteristics on build quality particularly in regard to densification.
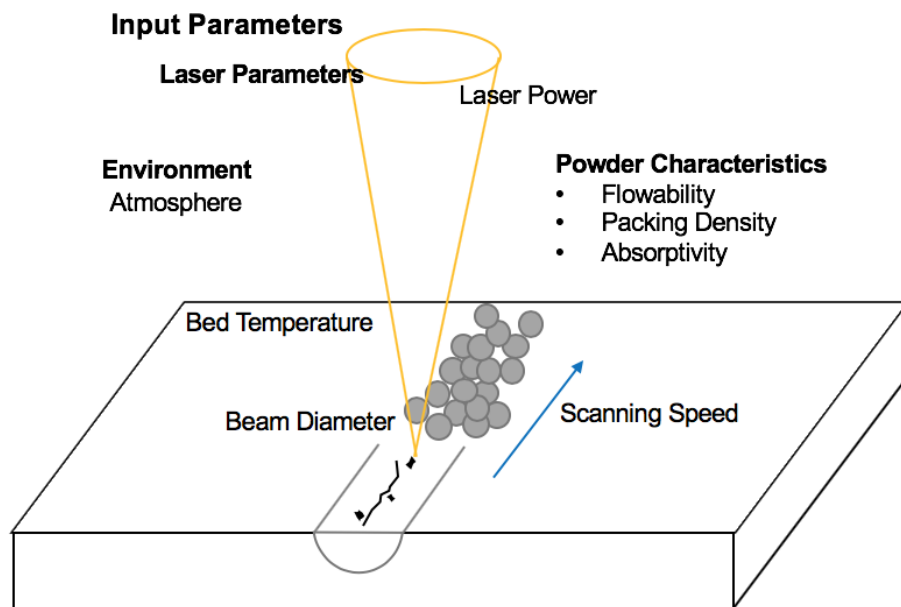

Figure 2 - Schematic diagram showing input parameters that will affect build quality

The characteristics of the powder play a significant role in the occurrence of defects within a part, and good flowability (free flowing coefficient, ff_c, >10) [14] and high packing density (> 60%) [15] are noted to improve overall quality in terms of prevalence of lack of fusion defects. The packing density of powders is known to be affected by their morphology with spherical powders having the highest packing density and irregularly shaped particles having a significantly lower one [16]. Lee and Zhang showed an increase in powder packing density increased the likelihood of a continuous melt track forming due to a more consistent powder layer preventing fluid instabilities and thus, balling [17]. Spherical powder particles also exhibit better flowability, giving more uniform layer spreading during LPBF production [18]. Egger et al., found that typical packing densities within a powder bed vary between 40 and 60% dependent on powder morphology, with more spherical morphologies increasing packing density [19]. Packing densities on the lower end of the spectrum will lead to less uniform heat input, asymmetrical shrinkage and greater irregularities in recoating powder in subsequent layers [18].

Although the laser power can be controlled and measured by machine settings, the actual heat input to the build will vary with the absorptivity of the powder. The absorptivity of tungsten powders and solid tungsten plate has been assessed theoretically and experimentally. These are summarized in Table 1, from which there is a lack of correlation and consistency in the values determined. As the

heat input will affect melting, consolidation and thermal profiles, a need exists to identify trends in this with powder and process characteristics, that can be correlated with final build quality.

Table I - Summary of reported laser absorptivity values

Study	Powder Morphology/ Preparation Method	Experimental Method	Absorptivity	Comments
Wang et al., 2017	Plasma Spheroidized	Temperature increase measured from insulated base plate with pre-deposited powder during laser irradiation	0.68	- Powder pre-deposited on plate not representative of LPBF - Temperature increases of <1000 K, well below melting point of tungsten
	Polyhedral		0.5	
Boley et al., 2016	Spherical (Gaussian Distribution)	Modelled - ray trace calculations of the laser through Fresnel reflections until power reaches 0.01% incident power	0.63	- Laser wavelength of 1 μm
	Flat Plate		0.4	
	Irregular	A thin layer of powder in a refractory metal disk ($\varnothing$ ~1 cm) with thermal insulation and thermocouples beneath the disk to measure temperature increase during laser irradiation	0.81	- Laser wavelength 970 nm - Layer thickness of 100 μm - Trapp et al., found increased powder thickness increase number of reflections and increase absorptivity
Trapp et al., 2017	Flat Plate	Temperature increase during laser irradiation measured on 0.5 mm thick disk of tungsten ($\varnothing$ 10 mm) within a porous alumina holder for thermal isolation with thermocouples attached to disk base	0.25 – 0.55	- Laser scanning speed 1500 mm/s - Power variation 50-500 W -Yb-fibre laser 65 μm -Absorptivity varied dependent on conduction or keyholing mode

Large flat surfaces or facets in the polyhedral powder used in the study by Wang et al. may more closely mimic a flat surface which Boley et al. predicted would have an absorptivity of 0.4 and was found experimentally to vary between 0.25 and 0.55 for 100 μm layers by Trapp et al., depending on laser power used and if the thresholds for melting or keyholing were achieved. Boley et al. conducted absorptivity measurements on titanium powders from different vendors but found no significant difference in absorptivity. However, if both powders were produced using the same method, variations in morphology and absorptivity are likely to be small [10, 20, 21]. Boley et al., found that the absorptivity of the powder tends to increase with the square root of the absorptivity of the flat surface.

The thermal conductivity in powders is significantly lower than that of the bulk material due to the ineffective conduction through the gas voids between the particles. Increasing the packing density was found to increase the thermal conductivity as there are often a greater number of particles in contact per unit area for conduction and therefore a smaller proportion of interparticle area [22].

As seen in Table I, thus far investigations into absorptivity have largely been limited to different packing distributions [21], materials and effect of LPBF process parameters on absorptivity. While a studies have investigated powder absorptivity of tungsten, the experimental limitations including the partial sintering of powder, larger layer thicknesses than typical LPBF systems may diminish its

applicability to LPBF fabrication [10]. Additionally, much of the energy absorbed will heat the powder to below the melting point of the material, which is ineffective to the LPBF process.

This study will therefore aim to provide a method to analyze the minimum effective energy absorbed from the two powders by analyzing build plate penetration. This negates the issue of non-representative powder packing and due to the comparative nature of the study, the effect of heat losses to the system are limited as the gas flow, plate thickness etc. and resulting conductive and convective losses will be comparable with both powder builds.

II. Experimental Method:

Sample Production:

Two different, high purity (<99.88 wt %) tungsten powders were used in this study, which were a chemically reduced (CR) powder supplied by H.C. Starck GmbH and a plasma spheroidised (PS) powder from LPW Technology Ltd., with nominal size distributions of <105 μm and 30 - 60 μm respectively. From manufacturer's specifications, the level of expected impurities in the powders are summarized in Table II and for which the level of oxygen is likely to have the most significant effect.

Table I – Maximum expected impurity levels (ppm)

	W	Al	Ca	Cr	Cu	Fe	Mo	Ni	Si	Ta	O
Chemically Reduced	bal.	30	20	100	10	200	100	150	50	-	170*
Plasma Spheroidized	bal.	-	-	10	-	10	30	10	-	30	370*

* determined via Inert Gas Fusion

Each powder was used to produce fourteen 10 x 10 x 10 mm^3 cubes using a narrow range of build parameters (duplicate builds of seven sets of parameters, Table III (with sample codes) laser power: 275 - 400 W; scan speed: 700 -1250 mms^{-1}; and scan spacing: 0.06 – 0.075 mm, which allowed location-specific variations to be assessed). These were produced on a Concept M2 Laser Cusing machine fitted with a 400 W laser under an argon atmosphere containing approximately 200 ppm of oxygen.

A 2 mm thick tungsten sheet (99.97 %) supplied by Plansee was cut to size and attached to a 90 x 90 mm titanium substrate plate using a high temperature metal adhesive to act as the build substrates for these cubes. The range of parameters used was selected to provide a range of heat inputs to the powders and have been quantified initially using the area energy density (AED).

AED is based on the laser power and the time needed to scan the entire area of the build plane, taking into account the overlap between scan tracks. In time δt, the laser would input an energy of P $δt$, and traverse a distance of v $δt$, see Figure 3.
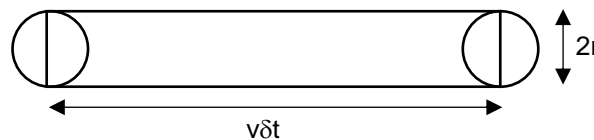

Figure 3 - Schematic representation of the laser scan parameters related to AED

So, in time δt, the area scanned by the laser corresponds to $2r \cdot v\delta t + \pi r^2$
As δt increases $2r \cdot v\delta t + \pi r^2 \rightarrow 2r \cdot v\delta t$
Therefore, the area energy density (Jmm^{-2}) was calculated using the following equation:

$$AED = \frac{P}{2rv}$$

Where P is laser power (W), v is laser scanning speed (mms^{-1}) and r is laser spot radius (mm)

Table II - Sample list and build parameters used

Sample Code	Powder	Power (W)	Laser Beam radius (μm)	Scan Speed (mm s^{-1})	Scan Spacing (mm)	AED (J mm^{-2})
PS-A	PS*	300	42	950	0.06	3.76×10^{-3}
PS-B	PS	300	42	750	0.06	4.76×10^{-3}
PS-C	PS	400	44.5	1250	0.06	3.60×10^{-3}
PS-D	PS	300	42	750	0.075	4.76×10^{-3}
PS-E	PS	300	42	850	0.06	4.20×10^{-3}
PS-F	PS	300	42	850	0.075	4.20×10^{-3}
PS-G	PS	275	40	700	0.06	4.91×10^{-3}
CR-A	CR*	300	42	950	0.06	3.76×10^{-3}
CR-B	CR	300	42	750	0.06	4.76×10^{-3}
CR-C	CR	400	44.5	1250	0.06	3.60×10^{-3}
CR-D	CR	300	42	750	0.075	4.76×10^{-3}
CR-E	CR	300	42	850	0.06	4.20×10^{-3}
CR-F	CR	300	42	850	0.075	4.20×10^{-3}
CR-G	CR	275	40	700	0.06	4.91×10^{-3}

* PS and CR represent the Plasma Spheroidized and Chemically Reduced powders respectively

Powder Characterization:
The oxygen contents in the two powders were determined via inert gas fusion using a LECO ONH836 machine, conducted by AMG Superalloys. A sample of material (0.1 - 0.12 g) was placed inside a graphite crucible with nickel flux. The sample was then fused releasing oxygen species which react with the carbon in the crucible to form carbon monoxide and carbon dioxide which was then detected and quantified using an NDIR (non-dispersive infrared) sensor [23].

The sizes of the particles were determined by Laser Particle Size Distribution (LPSD), conducted on a Sympatec GmbH HELOS system fitted with a SUCELL wet dispersing system in accordance with ASTM D4464 [24]. Given the expected size distribution of the powder an R2 lens with a detection range of 0.1 – 87.5 μm was used. $Na_4P_2O_7$ was added to the suspension of powder in distilled water to prevent agglomeration. The particle size distributions were confirmed via image analysis of backscattered electron (BSE) images obtained from a Hitachi TM3030 scanning electron microscope (SEM) operating at 15 kV. A visual investigation of the powder was also conducted to compare the morphology of the two powders; several images were taken at 100x to allow several hundred particles to be analyzed. Higher magnification images were taken to provide greater detail.

Shear ring testing was conducted on a Schulze Shear Ring Tester RST-01 fitted with a small cell (Type S). Instantaneous tests were performed in accordance with ASTM D6773 [25]. This test was used to determine ff$_c$ (free flowing coefficient) which is the ratio of consolidation stress to unconfined yield stress. A value greater than 10 for ff$_c$ is considered to be free-flowing and this is therefore the desired threshold for good powder flowability in LPBF [14].

The apparent (ρ_A) of the powders were also determined in accordance with ASTM B212 [26, 27]. The pack density term in LPBF is equivalent to the bulk or apparent densities of the powders. The value can also be as a percentage of the solid material (19300 kg m^{-3} for tungsten) for easier comparison especially between material systems.

Sample Characterization:
Following production, most samples were removed from the tungsten substrate plate using a wire EDM and subjected to Archimedes' density testing (ASTM B962) [28].
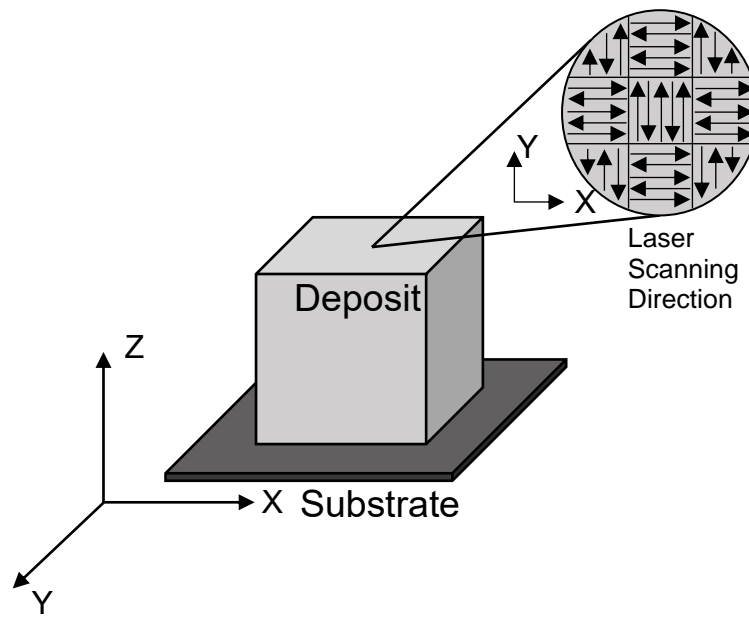
Figure 4 - Schematic showing the deposit and substrate, laser scanning directions and build orientations

The build orientations with respect to the substrate and deposit can been in Figure 4. Samples were then sectioned in the mid-plane, parallel to the substrate plate and polished to a 0.03 μm finish with colloidal silica (XY section). Defect quantification of the polished surfaces, as observed using an optical microscope (Zeiss Axioscop-2 equipped with Axiovision 4.6.3 image capture and analysis software), was conducted using Fiji software to determine the area fraction of defects on a binary image. Based on manual measurements of small lack of fusion defects, a threshold size of 1800 μm^2 was used, with defects larger than this determined to be lack of fusion defects, and those smaller determined to be cracks (see Figure 5) [29].
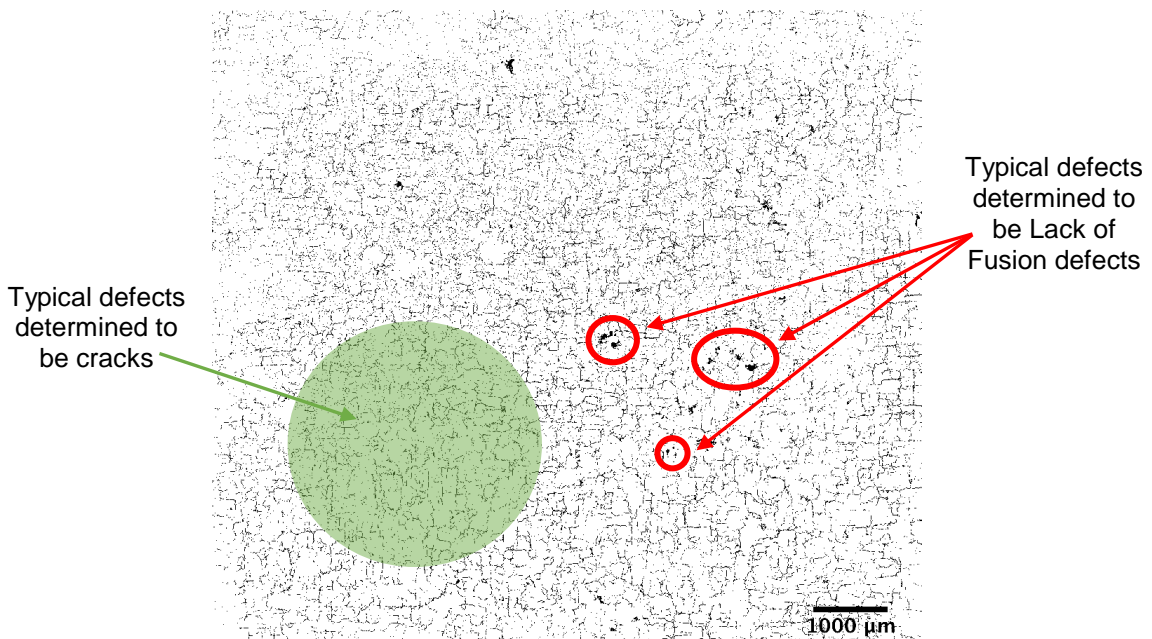

Figure 5 - Binary optical image showing defects; those larger than 1800 μm^2 determined to be Lack of Fusion defects, and those smaller determined to be cracks

A section was also taken perpendicularly through both substrate plate and deposit for samples CR-B and PS-B to determine the penetration depth of the fusion zones into the build plate for the two powder types (XZ section). These were taken from the same place in the build plate and were prepared in the same way for optical microscopy and image analysis. Measurements were taken manually using the lowest visible boundary between the parent material and the fusion zone from a datum of the substrate plate level away from the deposit at least every 0.5 mm using Fiji software across the width of the deposit [29], see Figure 6.
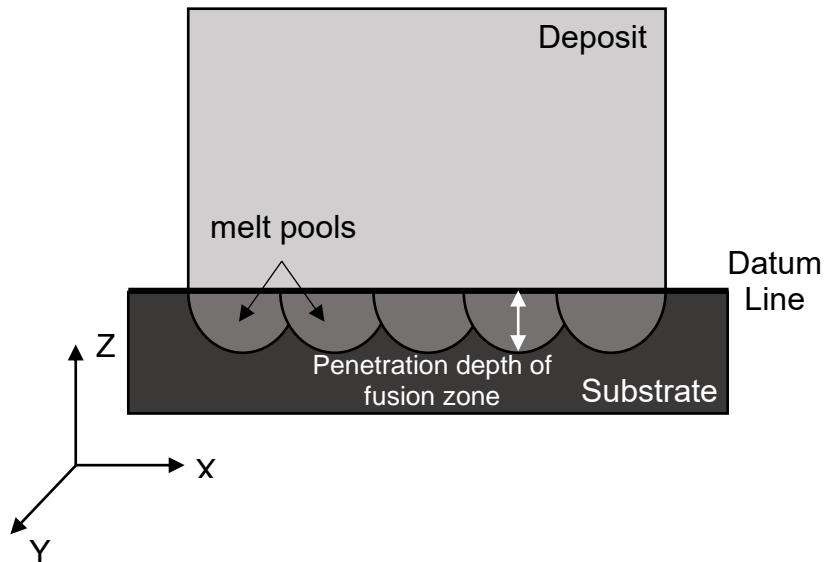

Figure 6 - Schematic of the build plate section showing penetration depth measurements taken

III. Results and Discussion:

Archimedes' density testing was conducted on the samples produced via LPBF; Figure 7 shows the variation of sample density as a function of AED.
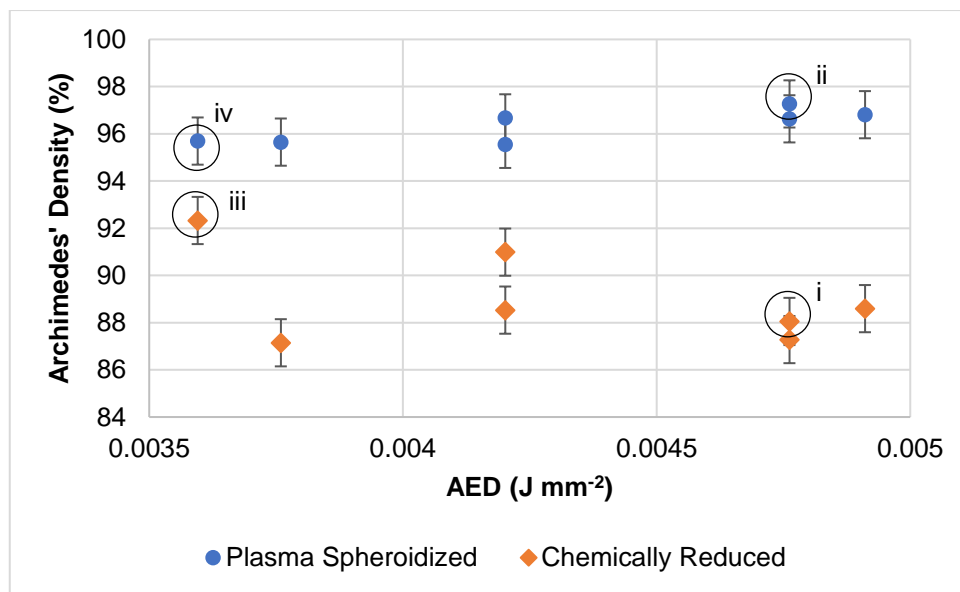

Figure 7 - Graph to show variation of sample density as a function of AED

As a narrow range of build parameters close to the optimum was used for the builds, there are only slight variations in sample density indicated in Figure 7. Indeed, the range from highest to lowest values for density was around 5 % for the chemically reduced powder and less than 2 % for the plasma spheroidized powder. Hence, no strong trends can be seen in terms of the effect of process parameters on sample density. However, whilst the density of the plasma spheroidized samples show

a weak increase with increasing AED, that for the compacts made from the chemically reduced powder deceases, resulting in the difference in density between compacts increasing from 4 to 10 % (those produced from the plasma spheroidized powder having the greater density).

From the measured densities, two conditions for each powder were identified for further study. These can be seen circled and labelled i) – iv) in Figure 7. The conditions of interest were those which yielded the highest densities for compacts from the plasma spheroidized and chemically reduced powders and the same parameters applied to the other powder type i.e. samples CR-B, PS-B, CR-C and PS-C. Of note, the optimum AED value for the compacts made from the plasma spheroidized powder corresponded to a power input of 300 W in comparison to the machine capability limit of 400 W required for compacts from the chemically reduced powder.

Archimedes' density testing does not identify the types of defect present, it merely gives an indication of overall build quality. To better understand the defect distributions in the compacts, mounted sections were imaged. Figure 8 shows micrographs typical for each of the samples of interest sectioned parallel to the build plate along with the densities determined by Archimedes' (AD) and Image Analysis (IA) methods, as well as an indication of the proportion of lack of fusion (F) and cracks (C) also determined through image analysis. Each pixel corresponds to 3 μm in the micrograph; each manual measurement is accurate to the nearest 2 pixels, and the manual measurements had a minimum size of 1800 μm^2, this corresponds to an error of approximately 0.5 %. The void type defects were determined to be lack of fusion rather than porosity due to their irregular shape, and large size. Gas or keyhole pores are typically spherical in shape. The high prevalence of large lack of fusion defects in i) may also lead to an increase in cracking as the defects may encourage crack initiation as their irregular shape could act as a stress concentrator. Both from the micrographs themselves and the values indicated from image analysis, it can be seen that the samples produced from the chemically reduced powder in Figure 8 i) and iii) have higher levels of lack of fusion whereas the plasma spheroidized samples ii) and iv) are dominated by cracking, but the absolute amount of cracking, likely occurring on cooling is consistent between 3 – 5 % throughout the samples. Under optimal conditions for this powder, the compacts produced from the plasma spheroidized powder can be considered to be nominally dense with only 0.3% lack of fusion voids. The quantity of cracking results in only 97 % theoretical density being achieved and likely occurs during the rapid cooling to which all samples were subjected rather than a parameter specific variation.
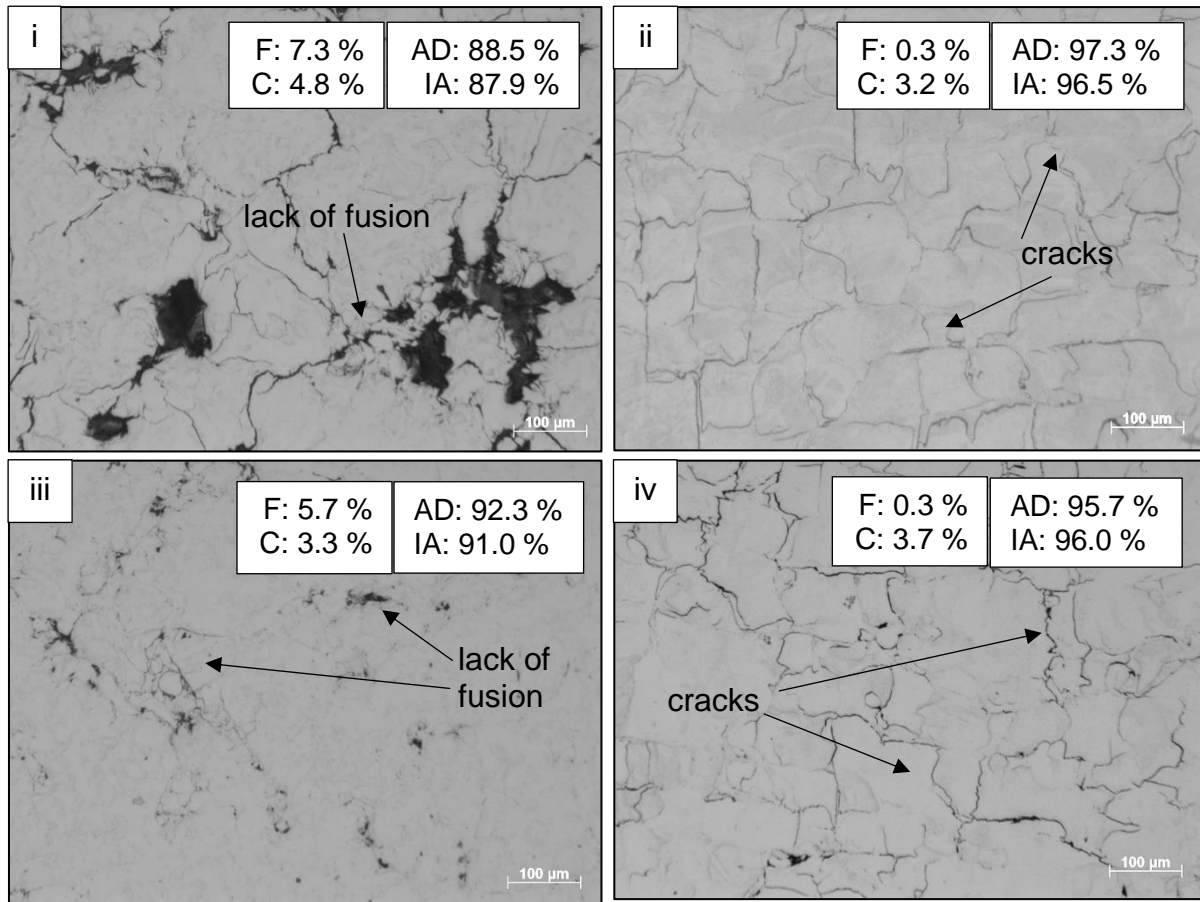
Figure 8 - Optical micrographs showing i) CR-B and ii) PS-B (optimized build parameters for plasma spheroidized powder) and iii) CR-C and iv) PS-C (optimized build parameters for chemically reduced powder)

Variation in packing density is likely to affect the thermal diffusivity and possibly the laser absorptivity as discussed in the introduction, with the experimental set-up and powder layer thickness having an effect on the packing density seen. In this study the two powders were found to have noticeably different characteristics in terms of packing and flowability (see Table IV); the improved flowability and higher packing of the spherical powder would be expected to result in improved build quality with higher density. From Figure 7, this can be confirmed, with the plasma spheroidized powder producing samples with consistently higher density. This is possibly due to the higher packing density resulting in greater contact between the particles allowing for more heat flow through the powder [16, 22].

Table III - Comparison of tungsten powders following characterisation

Powder	Apparent Density (g cm^{-3})	Percentage density (%)	ff$_c$
Plasma Spheroidized	11.06	57.0	11.04
Chemically Reduced	8.64	44.5	9.59

To confirm this, the penetration depths of the fusion zone into the substrate material were measured (see Figure 9 and Figure 10). The samples used for this were CR-B and PS-B respectively and therefore the build parameters were 300 W power, 750 mms^{-1} scanning speed and a scan spacing of 60 μm. The average penetration depth, excluding the edge 2mm, of the sample for the plasma spheroidized powder being 122 μm ± 10 compared with 67 μm ± 10 for the deposit produced from the chemically reduced powder, corresponding to a 1.8 times greater penetration for the plasma spheroidized deposit.

Underneath the sites of defects close to the base plate, the penetration depth is smaller due to reduced thermal conduction through the void (see dashed line). There is also some evidence of deeper penetration before and after the defect (see circled points) consistent with channeling of the heat through the solid material around the void, deepening the fusion zone. In Figure 11, this can be seen more clearly with penetration deepening on increasing distance from defect sites. In order to see this effect, the defect had to form very close to the substrate plate. In the deposit produced from the chemically reduced powder (Figure 10), two large lack of fusion defects can be seen (circled) but were too far away from the base plate to see the effect of channeling, whereas the much smaller lack of fusion defects (indicated by a square) showed some channeling.
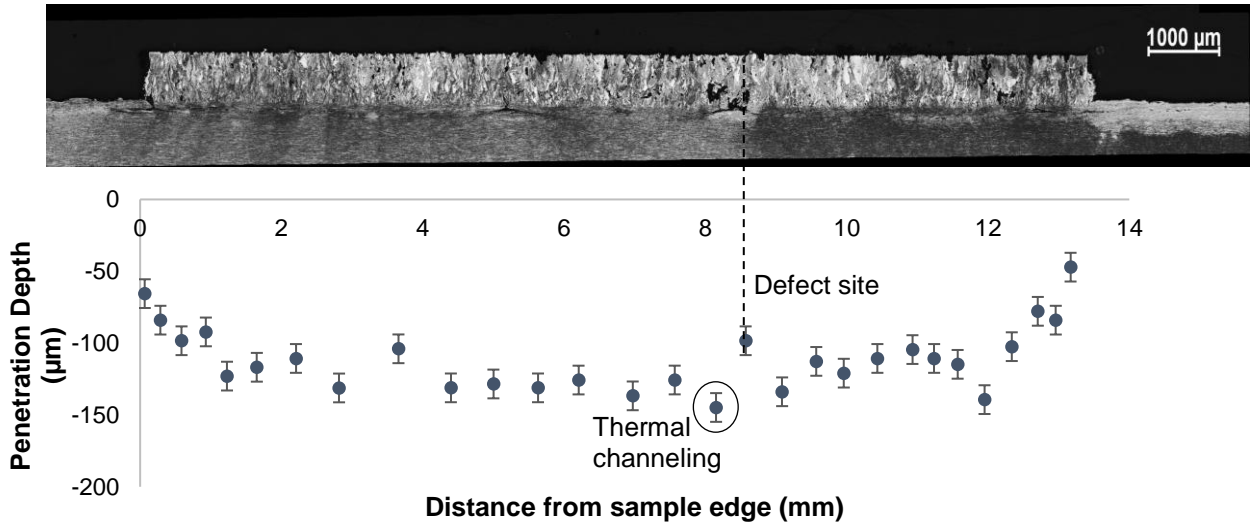
Figure 9 - Micrograph of section through the substrate plate and deposit produced using plasma spheroidized powder and the measured depth of the fusion zone at the corresponding position on the sample
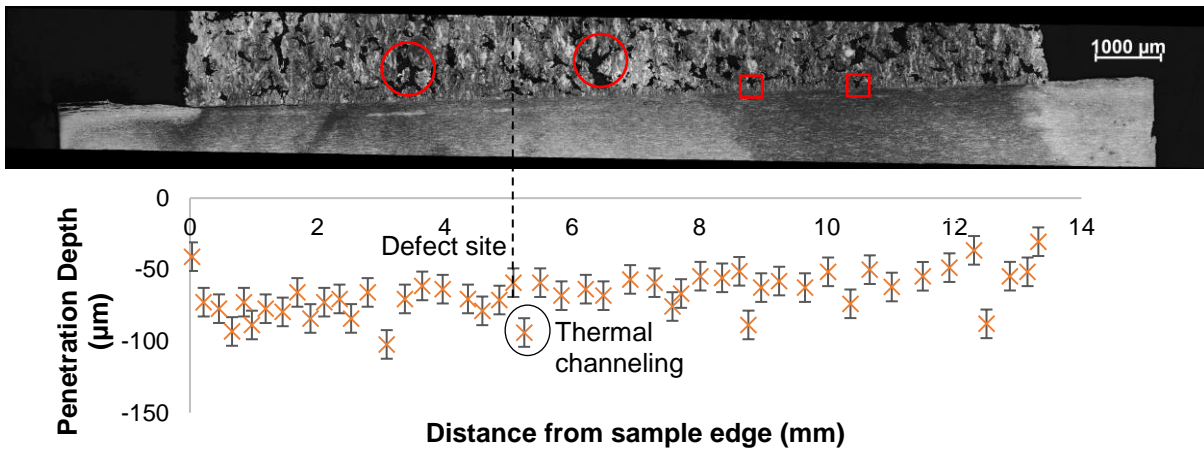

Figure 10 - Micrograph of section through the substrate plate and deposit produced using chemically reduced powder and the measured depth of the fusion zone at the corresponding position on the sample
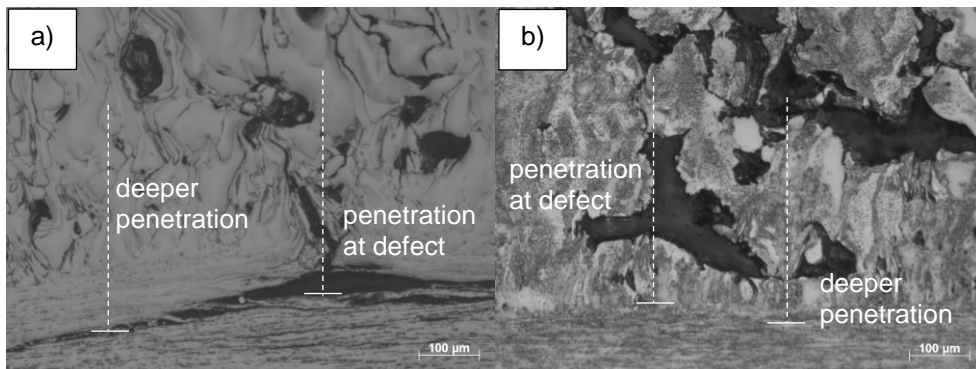

Figure 11 - Optical micrographs showing variation in penetration depth around areas of defects in a) plasma spheroidized powder and b) chemically reduced powder

The penetration depths are a measure of the fusion boundary for laser scanning of the first powder layer and, as such, is a measure of the heat absorbed by the powder from that layer.

Assuming that the region of average penetration is subject to one dimensional heat flow (vertically downward in Figure 9 and 10) then the penetration depth can be used as an estimate of the minimum heat input into the powder. This will be an under-estimate of the total heat input, but as the scan rates and overlaps are the same, the amount of heat required to raise the substrate temperature for $T < T_m$ will be the same for both powder types. The minimum heat absorption can be determined as a function of the total energy input by the laser.
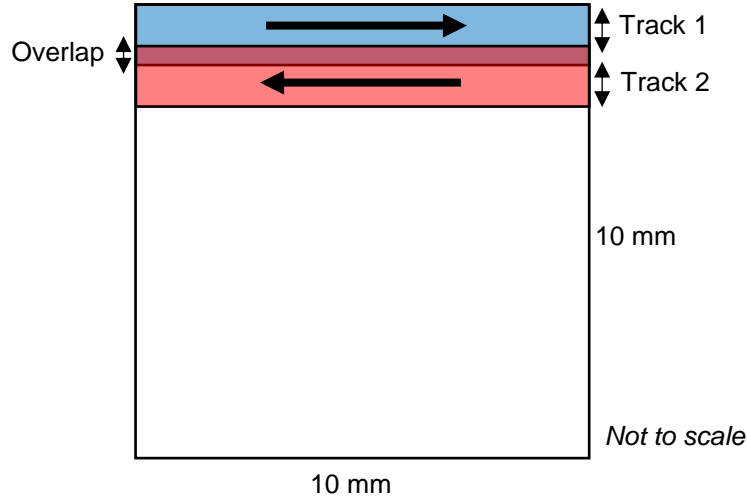
$$Area\ scanned = length\ of\ track\ \times\ no.tracks\ \times\ 2r$$
$$No.tracks = sample\ width \div scan\ spacing$$
$$\therefore\ Area\ scanned = 10\ \times\ \frac{10}{0.075}\ \times\ 0.084 = 112\ mm^2\ \equiv 1.12\ \times\ 10^{-4} m^2$$

The energy input over one layer, will be the product of the Area Energy Density (J m^{-2}) and the area (m^2)

$$E = \frac{P}{2rv}\ \times\ A$$
$$E = \frac{300}{2 \times (4.2 \times 10^{-5}) \times 0.75}\ \times\ (1.12\ \times\ 10^{-4})\ \approx\ 533\ J\ (3\ s.f.)$$

Thus, the incident energy of the laser approximates to 533 J (3 s.f.).

The average penetration depths, d, from the two powders, are then used along with the layer thickness, h, of the powder, the apparent, ρ_A and theoretical densities, ρ_T, of the powders and the layer area, A_{layer}, to determine the volume of the material where the maximum temperature was greater than or equal to its melting point.

$$V = A_{layer}\ \times\ (d + \left(h\ \times \frac{\rho_A}{\rho_T}\right))$$

For the plasma spheroidized powder, the volume was determined to be:

$$V = 1 \times 10^{-4} \times \left(1.22 \times 10^{-4} + \left(3 \times 10^{-5}\ \times \frac{11.06}{19.3}\right)\right) \approx 1.39 \times 10^{-8}\ m^3\ (3\ s.f.)$$

For the chemically reduced powder, the volume was determined to be:

$$V = 1 \times 10^{-4} \times \left(6.7 \times 10^{-5} + \left(3 \times 10^{-5}\ \times \frac{8.64}{19.3}\right)\right) \approx 8.04 \times 10^{-9}\ m^3\ (3\ s.f.)$$

Using the molar volume of tungsten, taken to be 9.55 x 10^{-6} m^{3}mol^{-1} [30], the number of moles, n, for the two powders were determined:

$$n_{PS} = \frac{V}{V_m} = \frac{1.39 \times 10^{-8}}{9.55 \times 10^{-6}} \approx 1.46 \times 10^{-3}\, mol$$
$$n_{CR} = \frac{V}{V_m} = \frac{8.04 \times 10^{-9}}{9.55 \times 10^{-6}} \approx 8.42 \times 10^{-4}\, mol$$

The change in enthalpy, H can be determined through the integration of the specific heat capacity, C_P, between the limits, T_m and T_O and the latent heat of fusion, L_f:

$$H = \int_{T_O}^{T_m} C_P\ \partial T + L_f$$

The specific heat capacity as a function of temperature was determined to be:

$$C_P = 0.0032426 \left(1 - \frac{4805}{T^2}\right) + (2.1773 \times 10^{-6})T + (5.52461 \times 10^{-13})T^3\ cal \cdot g^{-1} \cdot K^{-1} \text{ [31]}$$

The latent heat of fusion (L_f) was taken to be 46000 J mol^{-1} [30].

$$\int_{293}^{3695} C_P\ \partial T\ \approx 150.3\ cal \cdot g^{-1} \equiv 629.0\ J \cdot g^{-1} \equiv 115637.9\ J\ \cdot mol^{-1}$$

Assuming conversion factors of $1\ cal. \equiv 4.184$ J [32] and the atomic mass of tungsten of 183.84 J·mol^{-1} [30].

The enthalpy increase for the volumes of the two powders were found to be 236 J and 136 J (3 s.f.) for the plasma spheroidized and chemically reduced powders respectively. The relative minimum absorbed energies can then be compared to the incident energy of the laser in the two cases, 533 J. This results in a minimum absorption efficiency of 0.44 and 0.26 (2 s.f.) respectively.

The value of laser absorptivity will depend on material, powder characteristics (packing density and morphology) and processing environment [33]. The samples studies were processed under nominally identical conditions so that differences in effective laser absorptivity can be assumed to be due to powder composition, morphology and packing density. From Table II, the different powder compositions differ only in their impurity levels, so that, unless vaporization losses cause the local environment to vary and modify its interaction with the laser beam then it is the powder geometry that is responsible for this difference. Although easily vaporized metallic elements such as Al, Cu, and Mo are present and differ between the powders, their low levels justify this assumption that powder composition variations are not significant.

Morphology and packing of particles can alter the contact area between adjacent particles and hence the path for thermal conduction. Greater powder packing density (e.g. resulting from a more spherical morphology) would result in greater thermal diffusion.

Micrographs of the two powders, Figure 12, indicate significant differences in the morphology and size of the two powders. The chemically reduced powder was found to have an irregular, faceted morphology with flake and rod structures in addition to small satellite particles and agglomerates. The plasma spheroidized powder had a highly spherical morphology with some small irregularities present on the particle surface. As neither powder was produced from a gas atomization process, internal pores were not expected.

Both powders show similar size ranges (Figure 13), although there is a plateau in the distribution for the plasma spheroidized powder from around 6 to 20 μm; over this size range the chemically reduced powder has a cumulative percentage of 44. The greater proportion of fines would give a greater tendency to agglomerate, consistent with the SEM micrographs (Figure 12) along with the poorer flowability of the powder compared to the plasma spheroidized powder (Table IV). The poorer flowability shown by the chemically reduced powder would be expected to lead to greater variability of

powder packing in the powder bed, which will be discussed below. A wider size distribution might be expected to result in greater packing density, but the morphology effects outweigh this tendency resulting in lower apparent density values (see Table IV). The single density value, however, does not represent the likely range experienced in a powder bed.
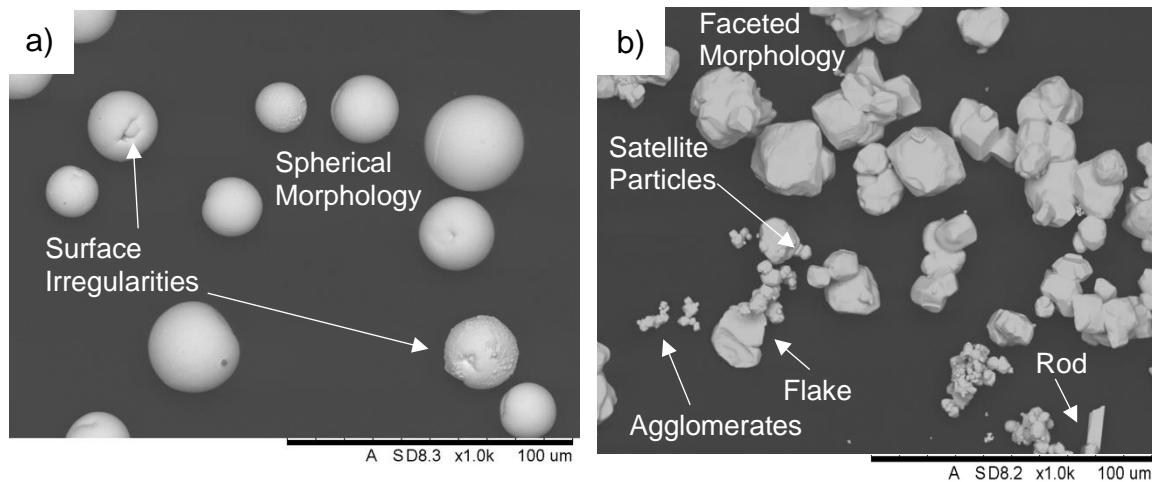

Figure 12 - Micrographs of a) the plasma spheroidized powder from LPW Technology and b) the chemically reduced powder from H.C. Starck

Higher density values are associated with higher thermal diffusivity values and so faster thermal transport in the plasma spheroidized powder build would be expected; the more insulating nature of the chemically reduced powder would then give higher temperatures in the powder layer. Analysis of the structure of the builds indicate that lack of fusion defects (see Figure 8) are more numerous for the chemically reduced powder build than for the plasma spheroidized powder build. Thus, although thermal diffusivity effects would lead to higher local temperatures for a similar heat input, the build microstructure is indicative that local temperatures in the chemically reduced build is lower than in the plasma spheroidized build, which is consistent with reduced heat input in the chemically reduced powder build. Hence, despite the broad assumptions of the analysis above, the minimum effective laser absorptivity values determined are indicative of a much-reduced intake of energy from the laser for the chemically reduced powder bed than for the plasma spheroidized powder.
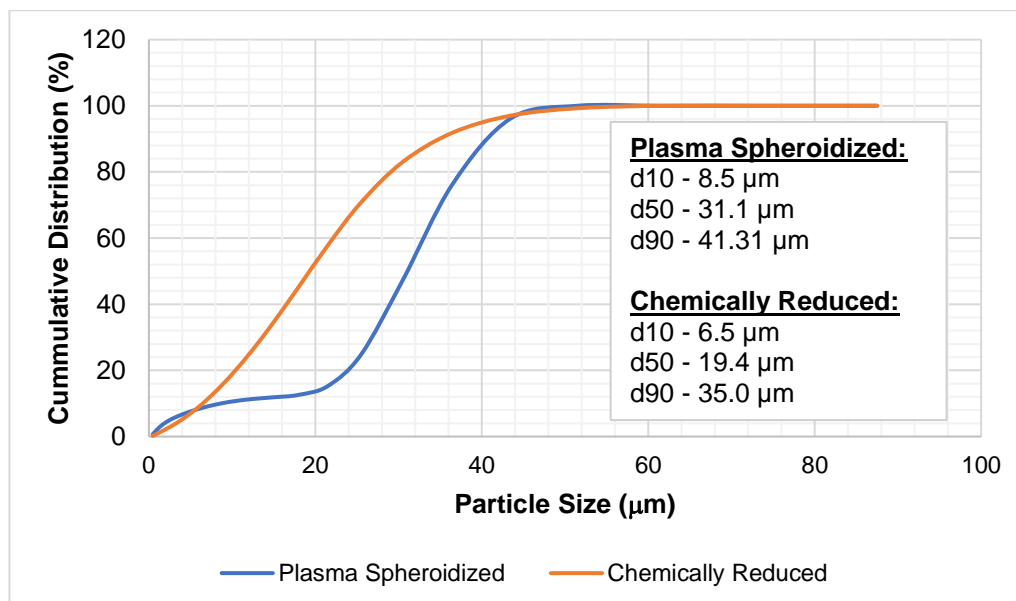

Figure 13 – Graph to show the size distribution of the plasma spheroidized and chemically reduced powders as determined by LPSD

The determined minimum absorbed efficiency of 0.26 and 0.44 for the chemically reduced and plasma spheroidized powders respectively were significantly lower than that of previous studies. This is likely due to the values only accounting for energy in melting rather than for all increases in substrate temperature (to less than that of the melting temperature). Additionally, the 30 μm layer thickness used during the fabrication process would lower the absorptivity in comparison to Trapp et al. where the layer thickness was three times greater allowing for multiple internal reflections.

Comparing the minimum effective absorptivity values for plasma spheroidized and chemically reduced powders, then the lower packing density of the latter would contribute to the decreased heat input [16, 22]. The importance of packing density can be inferred from the correlation between reduced penetration depth and large lack of fusion defects, (Figure 10). It is likely that the poorer flowability of the chemically reduced powder leads to reduced local packing density and hence reduced heat input. This results in less particle melting and so a lack of fusion defect whilst less heat is transported into the substrate, accounting for the reduced penetration.

The difference in apparent density, Table IV, is only 22 %, whilst that in the minimum laser absorptivity is 41 %, indicating that density is unlikely to fully account for the reduced heat input. Further to the modelling reported in the literature, the greater preponderance of facets in the chemically reduced powder would increase the amount of laser energy reflected back to the environment.

The trends seen, in terms of increased packing density increasing laser absorptivity and increased spheroidicity increasing laser absorptivity, are consistent between studies [10, 16, 20, 34] while absolute values vary significantly depending on morphology and size distribution. This indicates the morphology of the powder is a key factor in its absorptivity but also indicates a need to identify the absorptivity of the powder used in each study as literature values are inconsistent. It also highlights the need for further work in this area to clarify a consistent method for absorptivity measurements and thus improve comparisons of values between powders of different morphologies or different material systems.

IV. Conclusion:

Build plate analysis to determine the penetration depth of the fusion zone was used to compare the minimum effective energy absorbed between powders of the same material system. The melt penetration for the samples produced by the plasma spheroidized powder were almost double that of the chemically reduced powder and related to minimum absorption efficiencies of 0.44 and 0.26 respectively. This overcame some of the problems with previous laser absorption experiments which failed to produce representative packing.

The plasma spheroidized powder produced samples of enhanced quality with an average 7 % higher density than their chemically reduced counterparts over a range of parameters as a result of the enhanced absorbed energy. Variations in penetration depth have been related to adjacent lack of fusion defects and related to local density and heat input.

V. Acknowledgements:

VI. References:

1. PLANSEE, *Tungsten*, in *Plansee High Performance Materials*. 2017: Slough, U.K.
2. Taylor, N.P. and R. Pampin, *Activation properties of tungsten as a first wall protection in fusion power plants.* Fusion Engineering and Design, 2006. **81**(8): p. 1333-1338.
3. Savitskii, E.M. and G.S. Burkhanov, *Physical Metallurgy of Refractory Metals and Alloys*. 1970, New York: Consultants Bureau.
4. He, H., Y. Zeng, and N. Qu, *An investigation into wire electrochemical micro machining of pure tungsten.* Precision Engineering, 2016. **45**: p. 285-291.
5. Corti, C.W., *Sintering Aids in Powder Metallurgy - The Role of Platinum Metals in the Activated Sintering of Refractory Metals.* Platinum Metals Review, 1986. **30**(4): p. 184.
6. Li, R.D., et al., *Effects of processing parameters on rapid manufacturing 90W–7Ni–3Fe parts via selective laser melting.* Powder Metallurgy, 2010. **53**(4): p. 310-317.
7. Li, R., et al., *Selective laser melting W–10 wt.% Cu composite powders.* The International Journal of Advanced Manufacturing Technology, 2010. **48**(5): p. 597-605.
8. Faidel, D., et al., *Investigation of the selective laser melting process with molybdenum powder.* Additive Manufacturing, 2015. **8**: p. 88-94.
9. Zhang, D., Q. Cai, and J. Liu, *Formation of Nanocrystalline Tungsten by Selective Laser Melting of Tungsten Powder.* Materials and Manufacturing Processes, 2012. **27**(12): p. 1267-1270.
10. Wang, D., et al., *Dense Pure Tungsten Fabricated by Selective Laser Melting.* Applied Sciences, 2017. **7**(4): p. 430.
11. Iveković, A., et al., *Selective laser melting of tungsten and tungsten alloys.* International Journal of Refractory Metals and Hard Materials, 2018. **72**: p. 27-32.
12. Spierings, A.B., M. Schneider, and R. Eggenberger, *Comparison of density measurement techniques for additive manufactured metallic parts.* Rapid Prototyping Journal, 2011. **17**(5): p. 380-386.
13. Joyce, M., *Nuclear Engineering: A Conceptual Introduction to Nuclear Power*. 1st ed. 2017, Oxford, U.K.: Butterworth-Heinemann.
14. Schulze, D. *Flow Properties of Powders and Bulk Solids*. 2006; Available from: http://www.dietmar-schulze.com/grdle1.pdf.
15. Dullien, F., *Porous Media*. 2nd ed, ed. H. Brenner. 1991, Massachusetts, U.S.A. : Academic Press. 574.
16. Carr, R.L., *Evaluating Flow Properties of Solids.* Chemical Engineering Journal, 1965. **72**: p. 163-168.
17. Lee, Y. and W. Zhang, *Mesoscopic simulation of heat transfer and fluid flow in laser Powder bed additive manufacturing*, in *26th Solid Freeform Fabrication* 2015, University of Texas Austin: Texas, U.S. p. 1154-1165.
18. Tan, J.H., W.L.E. Wong, and K.W. Dalgarno, *An overview of powder granulometry on feedstock and part performance in the selective laser melting process.* Additive Manufacturing, 2017. **18**: p. 228-255.
19. Egger, G., et al., *Optimization of powder layer density in selective laser sintering*, in *Solid Freeform Fabrication Symposium*. 1999, University Texas Austin: Texas, U.S. p. 255-263-255-263.
20. Trapp, J., et al., *In situ absorptivity measurements of metallic powders during laser powder-bed fusion additive manufacturing.* Applied Materials Today, 2017. **9**(Supplement C): p. 341-349.
21. Boley, C.D., et al., *Metal powder absorptivity: modeling and experiment.* Applied Optics, 2016. **55**(23): p. 6496-6500.
22. Gusarov, A.V. and E.P. Kovalev, *Model of thermal conductivity in powder beds.* Physical Review B, 2009. **80**(2): p. 024202.
23. *Oxygen, Nitrogen, and Hydrogen in Refractory Metals*, L. Corporation, Editor. 2013: Michigan, U.S.A.
24. *Standard Test Method for Particle Size Distribution of Catalytic Materials by Laser Light Scattering*. 2015, ASTM International: West Conshohocken, PA.
25. *Standard Test Method for Bulk Solids Using Schulze Ring Shear Tester*. 2016, ASTM International: West Conshohocken, PA.
26. *Standard Test Method for Apparent Density of Free-Flowing Metal Powders Using the Hall Flowmeter Funnel*. 2013, ASTM International: West Conshohocken, PA.

27.   *Standard Test Method for Determination of Tap Density of Metal Powders and Compounds*.
       2015, ASTM International: West Conshohocken, PA.
28.   *Standard Test Methods for Density of Compacted or Sintered Powder Metallurgy (PM)*
       Products Using Archimedes' Principle. 2015, ASTM International: West Conshohocken, PA.
29.   Schindelin, J., et al., *Fiji: an open-source platform for biological-image analysis.* Nature
       Methods, 2012. **9**: p. 676.
30.   Lassner, E. and W.D. Schubert, *Tungsten: Properties, Chemistry, Technology of the Element,*
       Alloys, and Chemical Compounds. 1999, New York, U.S.: Plenum Publishers.
31.   Yih, S.W.H. and C.T. Wang, *Tungsten: Sources, Metallurgy, Properties, and Applications*.
       1979, New York: Plenum Press.
32.   Thompson, A. and B.N. Taylor, *Guide for the use of the International System of Units (SI)*.
       2008: Maryland, USA.
33.   Bergström, D., *The Absorption of Laser Light by Rough Metal Surfaces*, in *Applied Physics*
       and Mechanical Engineering. 2008, Luleå University of Technology: Österund, Sweden.
34.   Boley, C.D., S.A. Khairallah, and A.M. Rubenchik, *Calculation of laser absorption by metal*
       powders in additive manufacturing. Applied Optics, 2015. **54**(9): p. 2477-2482.